INTERNATIONAL JOURNAL FOR NUMERICAL METHODS IN FLUIDS, VOL. 27, 207–227 (1998)

# FINITE ELEMENT ANALYSIS OF DIRECTIONAL SOLIDIFICATION OF MULTICOMPONENT ALLOYS

S. D. FELICELLI,[1,2] J. C. HEINRICH[1]* AND D. R. POIRIER[3]

[1]*Department of Aerospace and Mechanical Engineering, The University of Arizona, Tucson, AZ 85721, U.S.A.*
[2]*Centro Atómico Bariloche, 8400 Bariloche, Argentina*
[3]*Department of Materials Science and Engineering, The University of Arizona, Tucson, AZ 85721, U.S.A.*

## SUMMARY

A finite element model of dendritic solidification of multicomponent alloys is presented that includes solutal convection and is an extension of a previously developed model for solidification of binary alloys. The model is applied to simulation of the solidification of ternary and quaternary Ni-based alloys. The role of solutal convection in the macrosegregation and the formation of freckles is analysed. Calculations show the effects of geometry and material properties on the convection patterns and the attendant segregation.

*Int. J. Numer. Meth. Fluids*, **27**, 207–227 (1998)

KEY WORDS: directional solidification; multicomponent alloys; dendritic monocrystals

## 1. INTRODUCTION

The demand for higher performance of gas turbines over the last several decades has prompted the development of new alloys and processes to achieve components resistant to creep at increasingly higher working temperatures.[1] The directional solidification of dendritic monocrystals has become the method of choice in casting turbine blades for high-temperature applications. In this process the casting is cooled from below in a vertically imposed temperature gradient in order to achieve a ⟨1 0 0⟩ orientation of the primary dendritic arms. However, the process is complicated by the onset of convection in the liquid phase, which can cause severe macrosegregation in the castings. A common defect is known as 'freckles', which are long, narrow streaks usually oriented parallel to the direction of gravity in the castings.[2] Their composition can vary significantly from that of the surrounding material, thus making the interfaces prone to the onset of fatigue cracking. The castings with freckles are scrapped.

The origin of freckles can be traced directly to the effect of solutal convection in the melt during directional solidification. Even though thermal convection may not occur in the process because the temperature profile is gravitationally stable, the rejection of a solute species lighter than the solvent at the solidifying interface can produce strong convection in the liquid, which leads to the formation of

---

*Correspondence to: J. C. Heinrich, Department of Aerospace and Mechanical Engineering, The University of Arizona, Tucson, AZ 85721, U.S.A.

Contract grant sponsor: Advanced Projects Research Agency; Contract grant number: MDA 972-93-2-0001
Contract grant sponsor: National Aeronautics and Space Administration; Contract grant number: NCC 8-96

CCC 0271–2091/98/010207–21 $17.50 *Received May 1996*

channels in the mushy zone and eventually freckles in the solidified casting. The dynamics of the process has been observed in transparent aqueous ammonium chloride solutions, which solidify in an analogous way to metals.[3,4]

Early numerical simulations to predict macrosegregation in alloys considered only convection in the mushy zone,[5–7] which was treated as a simplified porous medium. Formulations that incorporated solutal convection using the plane front assumption came next;[8,9] they could model convection in the liquid due to the rejection of solute at a planar solid–liquid interface. The first numerical models capable of simultaneously simulating convection in the all-liquid and mushy zones in binary alloys appeared next.[10–15] The extension of these models to multicomponent alloys has been accomplished only recently.[16–18] These models require a computational approach different from that for binary alloys because knowledge of the temperature in the mushy zone does not automatically provide a unique composition of the interdendritic liquid. Furthermore, the multicomponent nature of solidification can lead to convection and segregation patterns not previously observed in binary systems.

In this work we present a finite element model for the two-dimensional simulation of directional solidification of multicomponent alloys. We report on simulations performed for three- and four-component alloys and show how solutal convection affects the solidification process. We emphasize the effect of different modes of convection in the melt on the formation of freckles.

## 2. MATHEMATICAL MODEL OF SOLIDIFICATION

The model for the solidification of multicomponent alloys is an extension of the model for binary alloys previously developed by the authors.[15] A set of equations of conservation of mass, energy and solute concentration is solved in conjunction with the momentum equations for fluid flow. This is commonly known as a continuum model. The mushy zone is treated as a porous medium of variable porosity (i.e. volume fraction of liquid). The fraction of liquid varies from zero (all-solid region) to one (all-liquid region) in such a way that, when the volume fraction of liquid is zero, no fluid motion is possible and the system reduces to the energy equation. When the volume fraction of the liquid is one, the equations automatically become the Navier–Stokes and transport equations for an all-liquid region. The main assumptions used in the development of the governing equations are as follows.

1. Only solid and liquid phases may be present. No pores form.
2. The liquid is Newtonian and incompressible and the flow is laminar.
3. The solid and liquid phases have equal and constant physical properties.
4. There is no solute diffusion in the solid phase.
5. The Boussinesq approximation is made.
6. The solid phase is stationary.

Some further assumptions will be made at the appropriate places in the paper.

With the above simplifications the governing equations become

*continuity*

$$\nabla\cdot\mathbf{u}=0, \tag{1}$$

*momentum*

$$\phi\frac{\partial}{\partial t}\left(\frac{\mathbf{u}}{\phi}\right)+\nu_0\phi\mathbf{K}^{-1}\mathbf{u}-\nu_0\nabla^2\mathbf{u}+\frac{\phi}{\rho_0}\nabla p=-\mathbf{u}\cdot\nabla\left(\frac{\mathbf{u}}{\phi}\right)+\frac{\rho\phi}{\rho_0}\mathbf{g}, \tag{2}$$

*energy*

$$\frac{\partial T}{\partial t} - \alpha \nabla^2 T = -\frac{L}{c}\frac{\partial \phi}{\partial t} - \mathbf{u}\cdot\nabla T, \tag{3}$$

*conservation of solute components*

$$\frac{\partial \bar{c}^j}{\partial t} = \nabla\cdot D^j \phi \nabla c_1^j - \mathbf{u}\cdot\nabla c_1^j, \quad j = 1, \ldots, N. \tag{4}$$

In the above equations, $\nabla \equiv (\partial/\partial x)\hat{i} + (\partial/\partial y)\hat{j}$ is the gradient operator, $\mathbf{u} \equiv u\hat{i} + v\hat{j}$ is the velocity, $\phi$ is the volume fraction of liquid, $t$ is time, $v_0$ is the kinematic viscosity, $\rho_0$ is the reference density, $\mathbf{K}$ is the permeability, $p$ is the pressure, $\mathbf{g} \equiv g_x\hat{i} + g_y\hat{j}$ is gravity, $T$ is temperature, $\alpha$ is the thermal diffusivity, $L$ is the latent heat, $c$ is the specific heat, $\bar{c}^j$ is the total concentration of the alloy component $j$, $D^j$ is the diffusion coefficient of alloy $j$ in the liquid, $c_1^j$ is the concentration of the alloy component $j$ in the liquid phase and $N$ is the number of alloy components.

The density $\rho$ in the body force term is a function of the temperature and of the concentration of each of the alloy components, i.e.

$$\rho = \rho_0 \left( 1 + \beta_{\mathrm{T}}(T - T_{\mathrm{R}}) + \sum_{j=1}^{N} \beta_{\mathrm{c}}^j (c_1^j - c_{\mathrm{R}}^j) \right), \tag{5}$$

where $\beta_{\mathrm{T}} = (1/\rho_0)(\partial\rho/\partial T)$, $\beta_{\mathrm{c}}^j = (1/\rho_0)(\partial\rho/\partial c_1^j)$. $T_{\mathrm{R}}$ is the reference temperature and $c_{\mathrm{R}}^j$ are the reference concentrations of the alloy components at $\rho = \rho_0$.

The permeability in the momentum equations is expressed in the principal directions perpendicular and parallel to the primary dendrites, i.e.

$$\mathbf{K} = \begin{bmatrix} K_x & 0 \\ 0 & K_y \end{bmatrix},$$

and has been obtained from experimental data and calculations.[19,20] The permeability coefficients are expressed in terms of the primary dendrite arm spacing $d_1$ and the volume fraction of liquid, $\phi$, as

$$K_x = \begin{cases} 1{\cdot}09 \times 10^{-3} \phi^{3{\cdot}32} d_1^2, & \phi < 0{\cdot}65, \\ 4{\cdot}04 \times 10^{-6} \left( \dfrac{\phi}{1-\phi} \right)^{6{\cdot}7336} d_1^2, & 0{\cdot}65 \leqslant \phi < 0{\cdot}75, \\ \left[ -6{\cdot}49 \times 10^{-2} + 5{\cdot}43 \times 10^{-2} \left( \dfrac{\phi}{1-\phi} \right)^{0{\cdot}25} \right] d_1^2, & 0{\cdot}75 \leqslant \phi < 1, \end{cases} \tag{6}$$

$$K_y = \begin{cases} 3{\cdot}75 \times 10^{-4} \phi^2 d_1^2, & \phi < 0{\cdot}65, \\ 2{\cdot}05 \times 10^{-7} \left( \dfrac{\phi}{1-\phi} \right)^{10{\cdot}739} d_1^2, & 0{\cdot}65 \leqslant \phi < 0{\cdot}75, \\ 0{\cdot}074[\log(1-\phi)^{-1} - 1{\cdot}49 + 2(1-\phi) - 0{\cdot}5(1-\phi)^2] d_1^2, & 0{\cdot}75 \leqslant \phi < 1, \end{cases} \tag{7}$$

The total concentrations of the alloy components in the mixture, $\bar{c}^j$, and the concentrations of the components in the liquid phase, $c_1^j$, are related by

$$\bar{c}^j = \phi c_1^j + (1-\phi)\bar{c}_{\mathrm{s}}^j, \tag{8}$$

where $\bar{c}_{\mathrm{s}}^{j}$ is the average concentration in the solid phase and, in the case of no diffusion in the solid, is given by

$$\bar{c}_{\mathrm{s}}^{j} = \frac{1}{1-\phi}\int_{\phi}^{1} k^{j} c_{1}^{j}\,\mathrm{d}\phi. \tag{9}$$

Here $k^j$ are the equilibrium partition coefficients.

The model assumes that the liquidus temperature of the alloy in the mushy zone is a function of its local composition (no undercooling is allowed), which we express in the form

$$T = F(c_{1}^{j}). \tag{10}$$

We non-dimensionalize the equations using a reference length scale $H$ and a reference thermal gradient $G$, which are taken to be of the same order as the primary dendrite arm spacing and the initial temperature gradient respectively. The reference velocity, time and pressure are given respectively by

$$U = (g\beta_{\mathrm{T}}GH^{2})^{1/2}, \qquad \tau = \frac{H^{2}}{\nu_{0}}, \qquad P = \frac{\rho_{0}H^{2}}{\tau^{2}},$$

where $g$ is the magnitude of the gravitational acceleration.

The temperature is non-dimensionalized according to

$$T = \frac{T' - T_{\mathrm{R}}}{GH},$$

where $T'$ denotes the dimensional temperature, and the solute concentrations are non-dimensionalized with respect to $c_{\mathrm{R}}^{j}$.

The governing equations in non-dimensional form are:

*continuity*

$$\boldsymbol{\nabla}\cdot\mathbf{u} = 0, \tag{11}$$

*momentum*

$$\left(\frac{Pr}{R_{\mathrm{T}}}\right)^{1/2}\left[\phi\frac{\partial}{\partial t}\left(\frac{\mathbf{u}}{\phi}\right) - \nabla^{2}\mathbf{u} + \mathbf{Da}^{-1}\phi\mathbf{u}\right] = -\phi\left(\frac{Pr}{R_{\mathrm{T}}}\right)\boldsymbol{\nabla}p - \mathbf{u}\cdot\boldsymbol{\nabla}\left(\frac{\mathbf{u}}{\phi}\right) + \phi\left(\mathrm{sgn}(\beta_{\mathrm{T}})T + \frac{Pr}{R_{\mathrm{T}}}\sum_{j=1}^{N}\frac{R_{\mathrm{s}}^{j}}{Sc^{j}}[\mathrm{sgn}(\beta_{\mathrm{c}}^{i})c_{1}^{j} - 1]\right)\hat{\mathbf{g}}, \tag{12}$$

where $\hat{\mathbf{g}}$ is a unit vector in the direction of gravity,

*energy*

$$\frac{\partial T}{\partial t} - \frac{1}{Pr}\nabla^{2}T = -\hat{L}\frac{\partial\phi}{\partial t} - \left(\frac{R_{\mathrm{T}}}{Pr}\right)^{1/2}\mathbf{u}\cdot\boldsymbol{\nabla}T, \tag{13}$$

*conservation of solute components*

$$\frac{\partial\bar{c}^{j}}{\partial t} = \frac{1}{Sc^{j}}\boldsymbol{\nabla}\cdot\phi\boldsymbol{\nabla}c_{1}^{j} - \left(\frac{R_{\mathrm{T}}}{Pr}\right)^{1/2}\mathbf{u}\cdot\boldsymbol{\nabla}c_{1}^{j}, \quad j = 1,\ldots,N. \tag{14}$$

The governing non-dimensional parameters in (11)–(14) are

(a) $Pr = \nu_{0}/\alpha$, the Prandtl number

(b) $R_{\mathrm{T}} = g|\beta_{\mathrm{T}}|GH^4/v_0\alpha$, the thermal Rayleigh number
(c) $\mathbf{Da} = (1/H^2)/\mathbf{K}$, the Darcy tensor
(d) $R_{\mathrm{s}}^j = g|\beta_{\mathrm{c}}^j|c_{\mathrm{R}}^j H^3/v_0 D^j$, the solutal Rayleigh number for solute $j$
(e) $Sc^j = v_0/D^j$, the Schmidt number for solute $j$
(f) $\hat{L} = L/cGH$, the non-dimensional latent heat.

The velocity scale for natural convection has been chosen because it is convenient when body forces due to buoyancy dominate the convective motion, as is the case in the calculations that will be presented here. However, in the absence of strong gravity forces, as is the case under microgravity conditions in space where shrinkage and/or capillary forces drive the convection, this non-dimensionalization must be replaced by one in which the velocity scale reflects the appropriate convective mechanism.

## 3. FINITE ELEMENT MODEL

A successful numerical implementation of the solidification model presented in the last section requires some considerations and organization of the calculations, which we discuss below.

### 3.1. *Computation of Average Concentrations $\bar{c}_{\mathrm{s}}^j$ and $c_{\mathrm{l}}^j$*

From (9) we define

$$I_j \equiv \int_{\phi}^{1} k^j c_{\mathrm{l}}^j \, \mathrm{d}\phi = (1-\phi)\bar{c}_{\mathrm{s}}^j \tag{15}$$

and, using the trapezoidal rule, we can construct the recursive relation

$$I^{j,n+1} = I^{j,n} + \tfrac{1}{2}k^j(c_{\mathrm{l}}^{j,n} + c_{\mathrm{l}}^{j,n+1})(\phi^n - \phi^{n+1}), \tag{16}$$

where the superscript $n$ indicates the time level $t^n$ and we have assumed that the equilibrium partition coefficients $k^j$ are constant during a time step $t^n \leqslant t \leqslant t^{n+1}$ but vary with concentrations.

If remelting takes place at some point during the process, the values of $I^j$ must be obtained from the solidification history; hence

$$I^{j,n+1} = H^j(\phi^{n+1}), \tag{17}$$

where $H^j$ are the histories of solidification for each alloy component, stored at selected values of $\phi$ at every node in the mesh that has undergone solidification and interpolated linearly at values of $\phi$ different from the saved values.

From (8), (15) and (16), the following recursion relation is obtained that gives concentrations of the components in the liquid:

$$c_{\mathrm{l}}^{j,n+1} = \frac{\bar{c}^{j,n+1} - I^{j,n} - \frac{1}{2}k^j c_{\mathrm{l}}^{j,n}(\phi^n - \phi^{n+1})}{\phi^{n+1} + \frac{1}{2}k^j(\phi^n - \phi^{n+1})} \tag{18}$$

during solidification and

$$c_{\mathrm{l}}^{j,n+1} = \frac{\bar{c}^{j,n+1} - H(\phi^{n+1})}{\phi^{n+1}} \tag{19}$$

during remelting.

### 3.2. Calculating Volume Fraction of Liquid, $\phi$

The equations for $\bar{c}^j_s$ and $c^j_1$ derived above require knowledge of the fraction of liquid, $\phi$, at time $t^{n+1}$ if a node is in the mushy zone. In order to calculate $\phi$, we define the liquidus surface of the multicomponent alloy by writing equation (10) in the form

$$T_L = T_M + \sum_{j=1}^{N} \bar{m}^j c^j_1, \tag{20}$$

where $T_L$ denotes the liquidus temperature in the mushy zone and $T_M$ is the extrapolated melting temperature of the pure solvent. In general the coefficients $\bar{m}^j$ are functions of the local concentrations of the alloy components, $c^j_1$. In this work we assume that the $\bar{m}^j$ are constant.

From (8) and (15) we have

$$\bar{c}^j = \phi c^j_1 + I^j, \tag{21}$$

which we multiply by $\bar{m}^j$ and add over $j = 1, \ldots, N$ to obtain

$$\phi = \frac{\sum_{j=1}^{N} \bar{m}^j (\bar{c}^j - I^j)}{T_L - T_M} \tag{22}$$

after substituting equation (20). Notice that because $\bar{m}^j < 0$, $c^j_1 \geqslant 0$ and $I^j \geqslant 0$ for all $j$, satisfaction of (22) implies the satisfaction of (21) for each $j = 1, \ldots, N$.

In order to obtain a recursive relation for $\phi^{n+1}$, we substitute equation (16) into (22) to obtain

$$\phi^{n+1} = \frac{A^{n+1} - B^{n+1}\phi^n}{T^{n+1}_L - T_M - B^{n+1}}, \tag{23}$$

where

$$A^{n+1} = \sum_{j=1}^{N} \bar{m}^j (\bar{c}^{j,n+1} - I^{j,n}), \qquad B^{n+1} = \tfrac{1}{2} \sum_{j=1}^{N} \bar{m}^j k^j (c^{j,n+1}_1 + c^{j,n}_1).$$

When the eutectic temperature $T_E$ is reached, solidification proceeds isothermally until all the remaining eutectic liquid is solidified. Thus, at this stage, heat transfer is controlled by a balance between the heat released during solidification and thermal diffusion and convection. The strategy adopted in this case is to set $T = T_E$ at those nodes and to use the energy equation with the time-dependent term $\partial T/\partial t$ set equal to zero to calculate the volume fraction of liquid, i.e. we solve

$$\frac{\partial \phi}{\partial t} = \frac{c}{L} (\alpha \nabla^2 T - \mathbf{u} \cdot \nabla T). \tag{24}$$

The convective term in (24) may be neglected for alloys with a small fraction of eutectic liquid.

### 3.3. The Energy Equation

Fully implicit calculations are impractical because of the complexity of the model, so we resort to an iterative approach in which already-known values of some variables are used to update the remaining variables. This causes difficulties with the energy equation, which becomes unstable if the latent heat term is not calculated implicitly. The same problem was observed in modelling binary alloys,[14] but in that case a strategy different from the one presented here was employed to resolve it.

In order to obtain an equation in which the latent heat term is implicit and does not induce stability problems in the final algorithm, we first differentiate equation (21) with respect to time to obtain

$$\frac{\partial \bar{c}^j}{\partial t} = \phi \frac{\partial c_1^j}{\partial t} + c_1^j \frac{\partial \phi}{\partial t} + \frac{\partial I^j}{\partial t} \tag{25}$$

and then we approximate the time derivative of $I^j$ by

$$\frac{\partial I^j}{\partial t} = -k^j c_1^j \frac{\partial \phi}{\partial t} \tag{26}$$

using (16). Notice that equation (26) does not hold in the case of remelting. However, numerical experiments show that no significant errors are incurred with the use of (26) during remelting, as long as the time step remains reasonably small. On the other hand, the convergence properties of the algorithm deteriorate significantly and may be lost altogether if the term $\partial I/\partial t$ is treated explicitly. Substituting equation (26) into (25) and rearranging yields

$$(1 - k^j)c_1 \frac{\partial \phi}{\partial t} = \frac{\partial \bar{c}^j}{\partial t} - \phi \frac{\partial c_1^j}{\partial t}. \tag{27}$$

Multiplying by $m^j = \partial T/\partial c_1^j$ and summing over $j$, we obtain

$$\frac{\partial \phi}{\partial t} = \frac{\sum_{j=1}^{N} m^j \partial \bar{c}^j/\partial t - \phi \partial T/\partial t}{\sum_{j=1}^{N} (1 - k^j) m^j c_1^j}. \tag{28}$$

Finally, by substituting into (3), we obtain the final form of the energy equation as,

$$\left( 1 - \frac{L}{c} \frac{\phi}{\sum_{j=1}^{N} (1 - k^j) m^j c_1^j} \right) \frac{\partial T}{\partial t} - \alpha \nabla^2 T = -\mathbf{u} \cdot \nabla T - \frac{L}{c} \frac{\sum_{j=1}^{N} m^j \partial \bar{c}^j/\partial t}{\sum_{j=1}^{N} (1 - k^j) m^j c_1^j}. \tag{29}$$

Notice that equation (29) is not uniformly valid throughout the domain because it does not reduce to (3) when $\phi = 1$. Therefore the terms proportional to $L/c$ apply only to points in the mushy zone.

### *3.4. Finite Element Algorithm*

The dependent variables of velocity $\mathbf{u}$, temperature $T$ and total concentration of solute components, $\bar{c}^j, j = 1, \ldots, N$, are calculated from (2), (29) and (4) respectively using a penalty function, Petrov–Galerkin finite element formulation based on bilinear quadrilateral elements. The details of this procedure are contained in Reference 15 in the context of binary alloys and are not repeated here. However, we must mention that several other formulations have been implemented in an attempt to obtain more efficient algorithms for three-dimensional calculations. These include methods based on fractional steps[21,22] and stabilized equal-order methods,[23,24] which have been implemented with triangular and rectangular elements. Our results using these methods cannot be regarded as fully successful at this time and further development is needed before we can report on these efforts.

The rest of the dependent variables, the fraction of liquid, $\phi$, the solute concentrations in the liquid, $\bar{c}_1^j$, and the solute concentrations in the solid, $\bar{c}_s^j$, are calculated at each node using equation (23), equation (18) or (19) and equations (15) and (16) respectively. These variables are then interpolated using bilinear elements for use in the conservation and momentum equations.

The equations are solved sequentially and a partial iteration is performed within each time step to obtain convergence. The iteration does not include the momentum equations, which are solved only once at the beginning of the time step. At time $t^n$ all conditions are known. To advance to time $t^{n+1} = t^n + \Delta t$ whenever an equation is solved for one of the dependent variables, the latest available values for all other variables are used. The following path is taken in the calculations.

1. At time $t^n$ the dependent variables, $\mathbf{u}^n$, $T^n$, etc. are all known.
2. Set $t = t^{n+1}$ and $i = 0$, where $i$ is the iteration index.
3. Calculate $\mathbf{u}^{n+1}$ from (1), (2) and (5).
4. Calculate $T^{n+1}_{(i+1)}$ from (29).
5. Compare $T^{n+1}_{(i+1)}$ with $T_\mathrm{L}[(c^j_1)^{n+1}_{(i)}]$. If $T^{n+1}_{(i+1)} \leqslant T_\mathrm{L}[(c^j_1)^{n+1}_{(i)}]$ at a node, calculate $\phi^{n+1}_{(i+1)}$ at that node from (23).
6. For nodes where $\phi^{n+1}_{(i+1)} < 1$, calculate $(c^j_1)^{n+1}_{(i+1)}$ from (18) or (19).
7. Compute $(\bar{c}^j)^{n+1}_{(i+1)}$ from (4). (Note that $\bar{c}^j = c^j_1$ in the all-liquid region.)
8. Convergence check. If at every node we have $|\phi^{n+1}_{(i+1)} - \phi^{n+1}_{(i)}| < \varepsilon_1$ and $|(\bar{c}^j)^{n+1}_{(i+1)} - (\bar{c}^j)^{n+1}_{(i)} < \varepsilon_2$, then calculate $\bar{c}^{j,n+1}_\mathrm{s}$ and $I^{j,n+1}$ from (15) and from (16) or (17) respectively; set $T^{n+1} = T^{n+1}_{(i+1)}$, $\phi^{n+1} = \phi^{n+1}_{(i+1)}$, etc.; set $n = n + 1$ and go to step 2. Otherwise, set $i = i + 1$ and go to step 4.

The fraction of liquid and the mixture concentrations of the alloy solutes have been determined to be the most sensitive variables in the calculation and are used therefore to determine convergence ($\varepsilon_1$ and $\varepsilon_2$ are user-determined tolerances; in this work, $\varepsilon_1 = \varepsilon_2 = 10^{-5}$). On the other hand, the velocities are not sensitive to small changes in the rest of the variables and are calculated only once per time step.[25] Further details on the algorithm related to the treatment of remelting and solidification at the eutectic temperature have been given in Reference 15, where the selection of the time step and meshing strategies have also been discussed.

## 4. RESULTS AND DISCUSSION

We present here the results of simulations of the solidification of Ni-based superalloys. The boundary conditions are shown in Figure 1 for a rectangular domain; the same boundary conditions are used in the domains with variable vertical cross-sections that are introduced later. The calculations were performed with two alloys—a ternary mixture of Ni–Al–Ta with a composition of 5·8 wt.% Al, 15·2 wt% Ta and the rest Ni and a quaternary mixture of Ni–Al–Ta–Cr with a composition of 6 wt.% Al, 6 wt% Ta, 8 wt.% Cr and the rest Ni. The physical properties used in the calculations are given in Table I.

The simulations start with an all-liquid alloy of the nominal composition in a stable initial vertical temperature gradient such that at time $t = 0$ the bottom temperature is slightly above the alloy's melting temperature $T_\mathrm{R}$. At time $t = 0$ a constant cooling rate $r$ is applied at the bottom of the container and a constant temperature gradient $G$ is imposed at the top. Also at $t = 0$ a small random perturbation is introduced in the solute concentration fields in order to excite the convective motion. The simulations can then proceed until the whole domain is solidified.

### 4.1. Solidification in a Rectangular Enclosure (Case 1)

First we present simulations in a rectangular domain of width 7 mm and height 20 mm, discretized with a uniform mesh of $40 \times 60$ bilinear rectangular elements. We discuss two calculations with the ternary alloy Ni–Al–Ta of the above-mentioned composition, solidified with an initial temperature gradient $G = 2000$ K m$^{-1}$ at the rate $r = -0{\cdot}28$ K s$^{-1}$.

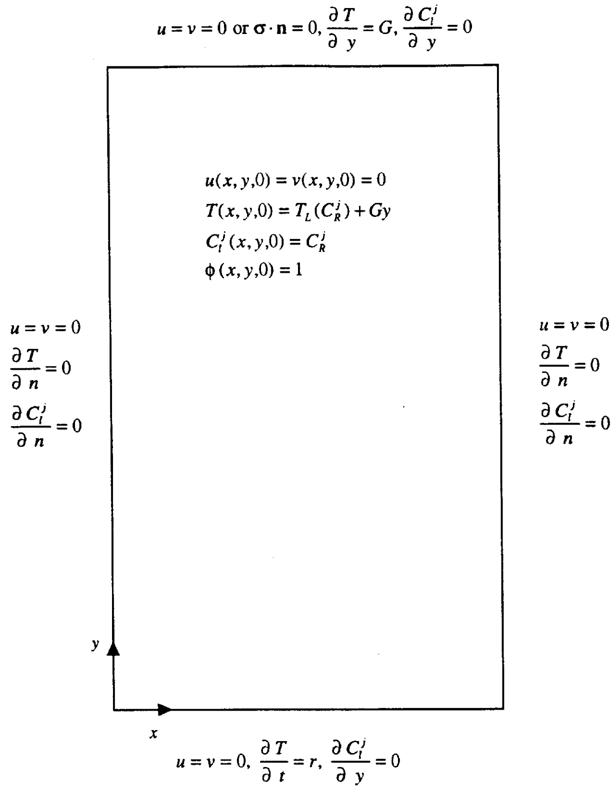

Figure 1. Rectangular domain showing initial and boundary conditions

Results for Case 1 are shown in Figures 2 and 3 after 80 and 200 s of solidification respectively. Figure 2(a) shows the volume fraction of liquid and indicates that the leading part of the mushy zone has advanced about 7·5 mm during this time; the bottom of the container is about 50% solid. A very-well-defined channel can be observed close to the midsection, which is all liquid starting about 3 mm from the bottom. Figure 2(b) shows the velocity field in the solidifying alloy. A plume is emanating from the channel into the all-liquid zone, causing two relatively strong convection cells in the liquid that entrain into the mushy zone to feed the plume. The maximum velocity in the liquid is of the order of 4·6 mm $s^{-1}$. Notice that the plume turns before reaching the top of the container. This is due to the stabilizing effect of the temperature gradient, which eventually stops the upward motion and forces the fluid to turn. The fluid motion within the mushy zone causes convective transport of lighter aluminium-rich fluid to the channel, as shown in Figure 2(c), lowering the density of the fluid within the channel and causing it to rise. Sharp concentration gradients develop along the channel walls between the aluminium-rich plume and the depleted neighbouring mushy zone, as shown in Figure 2(c). The effect of convection in the all-liquid zone can also be observed. The other component, Ta, does not contribute to convection since it increases the density of the liquid and is therefore a stabilizing agent when solidification is effected from below.

Figure 3(a) shows that after 200 s the leading part of the mushy zone has advanced about 17 mm and four channels are now evident—two along the walls of the mould and two in the interior of the casting. The latter have turned to the left and eventually merge with the channel developed along the left wall. The channel in the middle remains almost completely liquid from 3 to 7 mm high, but it is

Table I. Thermodynamic and transport properties used in simulations

| Property | Reference(s) |
|---|---|
| Reference concentrations | |
| Case 1: $c_R^{Al} = 5\cdot8$ wt.% Al; $c_R^{Ta} = 15\cdot2$ wt.% Ta | — |
| Cases 2–5: $c_R^{Al} = 6\cdot0$ wt.% Al; $c_R^{Ta} = 6\cdot0$ wt.% Ta; $c_R^{Cr} = 8\cdot0$ wt.% Cr | — |
| Reference temperatures | |
| Case 1: $T_R = 1685$ K | 26 |
| Cases 2–5: $T_R = 1691$ K | 26, 27 |
| Eutectic temperature: $T_E = 1560$ K | 28 |
| Extrapolated melting point of solvent:[a] $T_M = 1754$ K | — |
| Equilibrium partition ratios | |
| Case 1: $k^{Al} = 0\cdot54$; $k^{Ta} = 0\cdot48$ | 28 |
| Cases 2–5: $k^{Al} = 0\cdot89$; $k^{Ta} = 0\cdot61$; $k^{Cr} = 1\cdot0$ | 29 |
| Changes of liquidus temperature ($m^j = \partial T_L/\partial c_l^j$) | |
| $m^{Al} = -5\cdot17$ K (wt.% Al)$^{-1}$ | 27 |
| $m^{Cr} = -2\cdot11$ K (wt.% Cr)$^{-1}$ | 27 |
| $m^{Ta} = -2\cdot55$ K (wt.% Ta)$^{-1}$ | 27 |
| Thermal expansion coefficient: $\beta_T = -1\cdot15 \times 10^{-4}$ K$^{-1}$ | 30 |
| Solutal expansion coefficients | |
| $\beta_c^{Al} = -2\cdot26 \times 10^{-2}$ (wt.% Al)$^{-1}$ | 30 |
| $\beta_c^{Cr} = -2\cdot26 \times 10^{-3}$ (wt.% Cr)$^{-1}$ | 30 |
| $\beta_c^{Ta} = 3\cdot82 \times 10^{-3}$ (wt.% Ta)$^{-1}$ | 30 |
| Viscosity: $\mu = 4\cdot90 \times 10^{-3}$ N s m$^{-2}$ | 31 |
| Specific heat: $c = 660$ J kg$^{-1}$ K$^{-1}$ | 31 |
| Latent heat: $L = 2\cdot90 \times 10^5$ J kg$^{-1}$ | 31 |
| Thermal conductivity:[b] $\kappa = 80$ W K$^{-1}$ m$^{-1}$ | 32 |
| Density | |
| Case 1: $\rho_0 = 7365$ kg m$^{-3}$ | 30 |
| Cases 2–5: $\rho_0 = 6900$ kg m$^{-3}$ | 30 |
| Diffusion coefficient in liquid: $D = 5 \times 10^{-9}$ m$^2$ s$^{-1}$ | — |

[a] Extrapolated melting point of solvent is based on the liquidus temperature given by $T_L = 1685 - 2\cdot11c_l^{Cr} - 2\cdot55(c_l^{Ta} - 15\cdot18) -5\cdot17(c_l^{al} - 5\cdot81)$, where 1685 K is from Reference 26 for Ni–15·18 wt.% Ta–5·81 wt.% Al and the coefficients are from Reference 27.

[b] Extrapolation of the thermal conductivity of solid nickel to its melting point.[32]

closing from there up, leaving a pocket of liquid behind. If this process continues, eventually no liquid can flow to this pocket to offset the shrinkage due to the density change of solidification; this leads to the formation of porosity. Our model in its present state is not capable of modelling such situations; however, an extension is currently being implemented and the capability will be available in the near future.

In Figure 3(b) we have shown only the flow in the channels within the mushy zone; flow in the central channel is still significant, with a maximum speed of 0·2 mm s$^{-1}$, and accounts for the strong segregation and neighbouring depletion of aluminium observed in Figure 3(c). The interior channel on the right shows negligible convection motion and is therefore less segregated. The upper parts of the channels next to the walls show upward velocities and liquid entrainment into the mushy zone. Figure 3(c) shows that the aluminium component in the remaining liquid has been enriched by the convection. The bottom of the container shows some aluminium depletion.

This example illustrates the basic mechanisms in the formation of freckles and general macrosegregation in vertically solidified casts; in particular, the strongly non-linear interactions between the flow field, concentration fields and volume fraction of liquid in the mushy zone are apparent. The next example serves to illustrate the interaction between the temperature- and solutal-

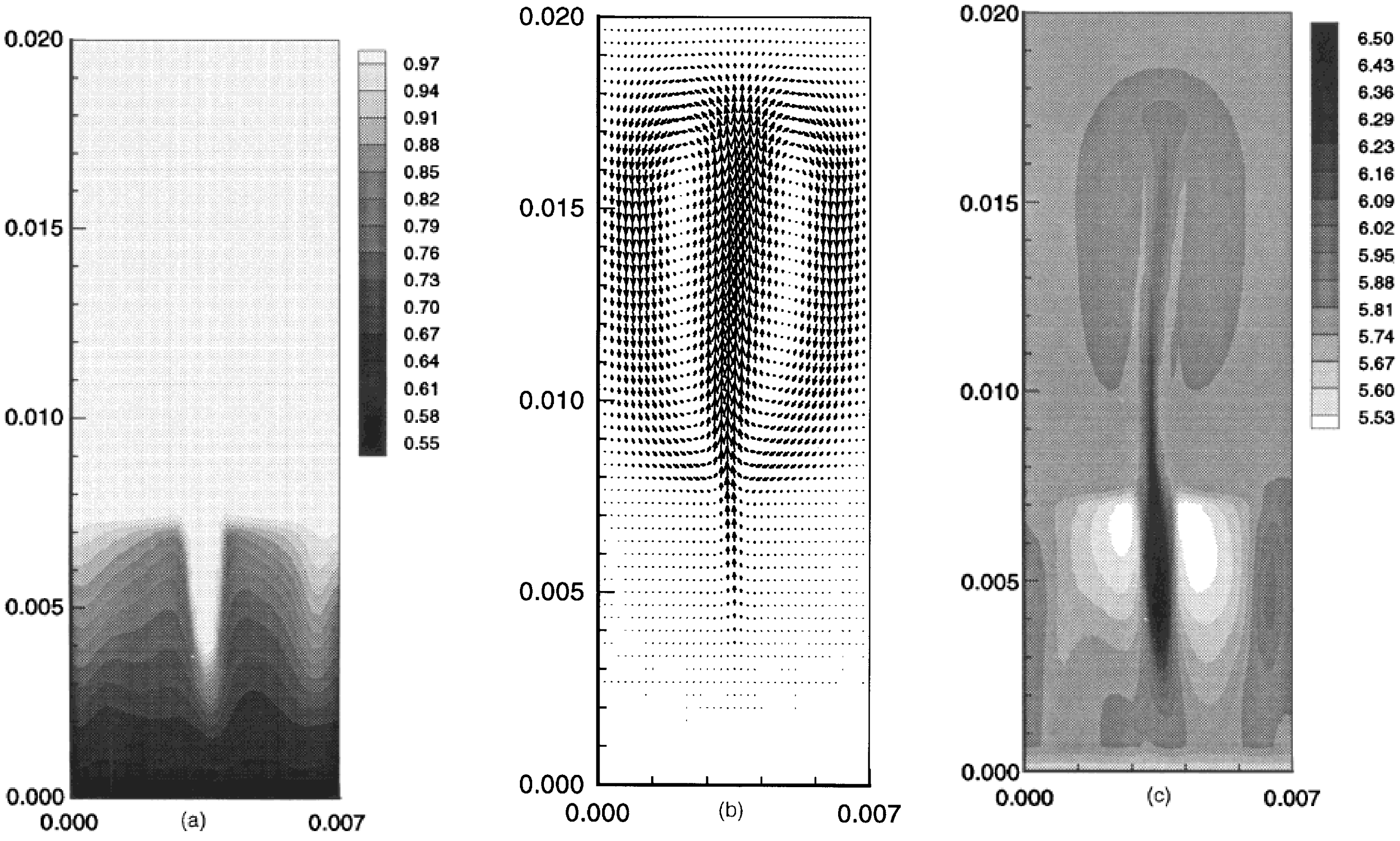

Figure 2. Solidification of Ni–5·8 wt.% Al–15·2 wt.% Ta in a rectangular enclosure after 80 s: (a) fraction of liquid; (b) velocity field (maximum velocity 4·6 mm $s^{-1}$), (c) mixture concentration of wt.% Al. Dimensions in metres

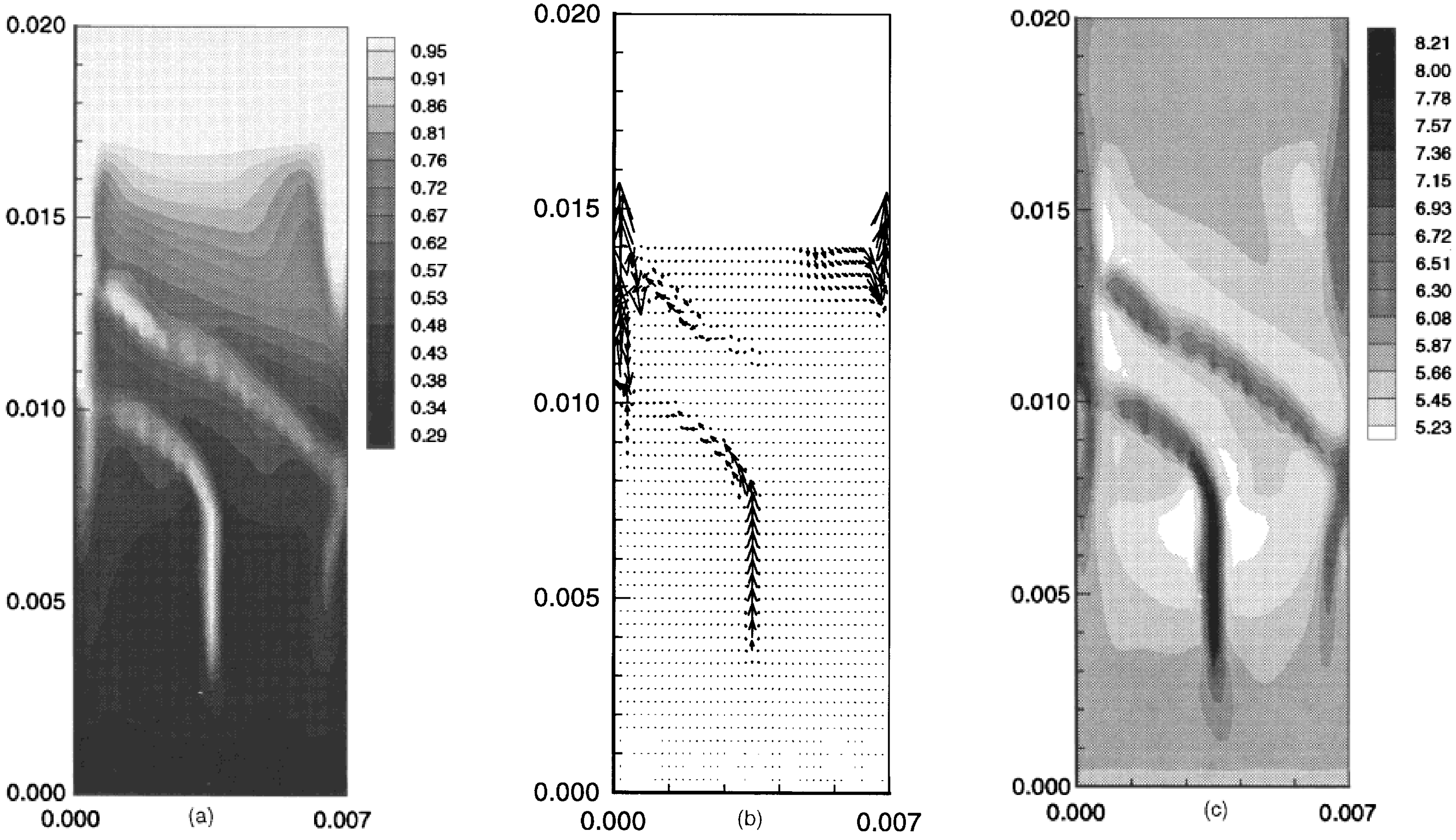

Figure 3. Solidification of Ni–5·8 wt.% Al–15·2 wt.% Ta after 200 s: (a) fraction of liquid; (b) velocity field in mushy zone (maximum displayed velocity 0·7 mm $s^{-1}$); (c) mixture concentration of wt.% Al. Dimensions in metres

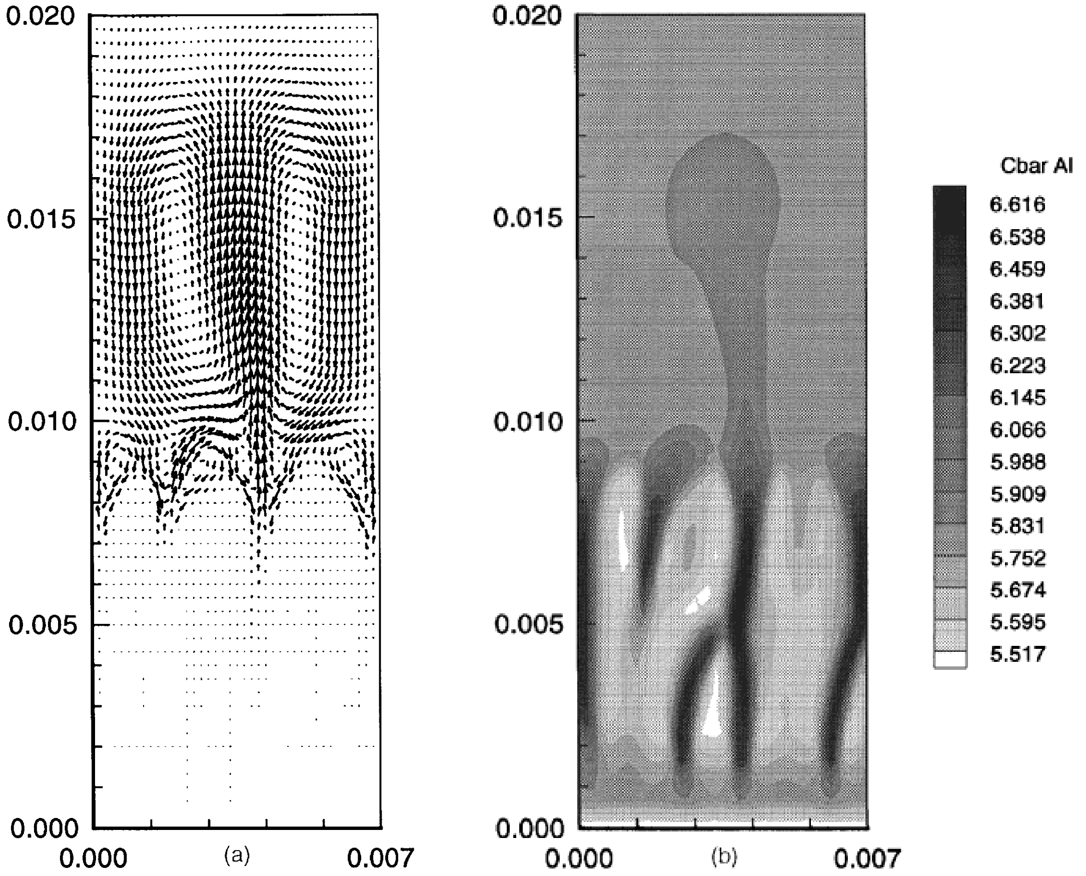

Figure 4. Solidification of Ni–5·8 wt.% Al–15·2 wt.% Ta with $k^{\mathrm{Al}} = 0{\cdot}75$ after 200 s: (a) flow field (maximum velocity 0·25 mm s$^{-1}$), (b) mixture concentration of wt.% Al. Dimensions in metres

driven flows and to emphasize the necessity of an accurate database if calculations of this type are to be used as a predicting tool. In particular, the importance of using accurate values of the partition coefficients $k^j$ is illustrated.

In the simulations of Figures 2 and 3, $k^{\mathrm{Al}} = 0{\cdot}54$ (obtained from Reference 29) was used; however, it is not clear that this represents an accurate estimate of $k^{\mathrm{Al}}$ and some evidence exists supporting higher values of the equilibrium partition ratio.[29] A calculation using $k^{\mathrm{Al}} = 0{\cdot}75$ and keeping the rest of the parameters the same as before is shown in Figure 4 after 200 s of solidification. Figure 4(a) shows the flow field and the presence of four channels where liquid is being ejected from the mushy zone, which has reached only 7 mm during this time. The flow entrains deep into the all-liquid region in only one of these locations; the other three turn quickly above the mushy zone and the flow in the liquid is dominated by two large cells streaming from the dominant channel. The concentration of aluminium in Figure 4(b) shows that a channel has formed and merged with the main channel deep in the mushy zone and that a channel started forming later than the others closer to the top of the mushy zone. These channels are relatively straight and the possibility of them bending and migrating across the domain, as in Figure 3(c), does not occur. The magnitude of the macrosegregation is also much smaller than in the previous case and overall convection is weaker, as expected, with a maximum velocity of 0·25 mm s$^{-1}$.

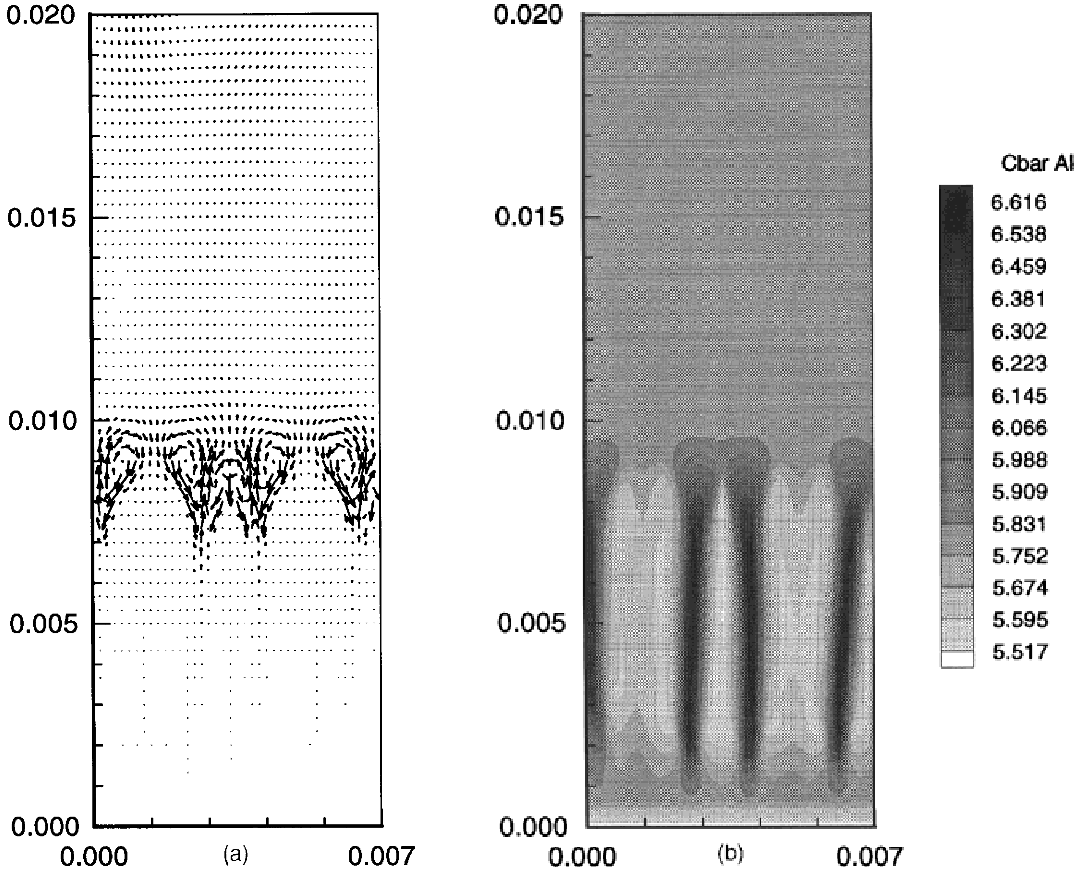

Figure 5. Solidification of Ni–5·8 wt.% Al–15·2 wt.% Ta with $k^{\mathrm{Al}} = 0{\cdot}77$ after 200 s: (a) flow field (maximum velocity 0·1 mm $\mathrm{s}^{-1}$), (b) mixture concentration of wt.% Al. Dimensions in metres

We now change $k^{\mathrm{Al}}$ to 0·77 for the same calculation. Results at 200 s are given in Figure 5 and show very significant changes. In Figure 5(a) none of the four channels in the mushy zone is strong enough to drive the fluid in the all-liquid region; convection is relegated to the upper part of the mushy zone and a small layer in the overlying liquid. Four channels started forming early on and remain very stable (in fact, they persist until solidification is complete), causing very straight and weakly segregated streaks that run through almost the entire casting. The maximum velocities here are of the order of 0·1 mm $\mathrm{s}^{-1}$ and segregation only amounts to less than 0·8 wt.% of the initial concentration of aluminium. This example underscores the importance of accurately measuring the equilibrium partition coefficients; in this case a 2·5% change in the value of $k^{\mathrm{Al}}$ has caused an important change in the mode of convection in the melt during solidification and in the macrosegregation patterns.

### 4.2. *Solidification in Enclosures with Smoothly Varying Geometry (Cases 2 and 3)*

We now turn our attention to the effect of geometry on the solidification process. Two simulations, one in a smoothly converging enclosure and the other in a diverging enclosure, are shown. Here the quaternary Ni–Al–Ta–Cr alloy is solidified. The temperature gradient is 5000 K $\mathrm{m}^{-1}$ and the cooling

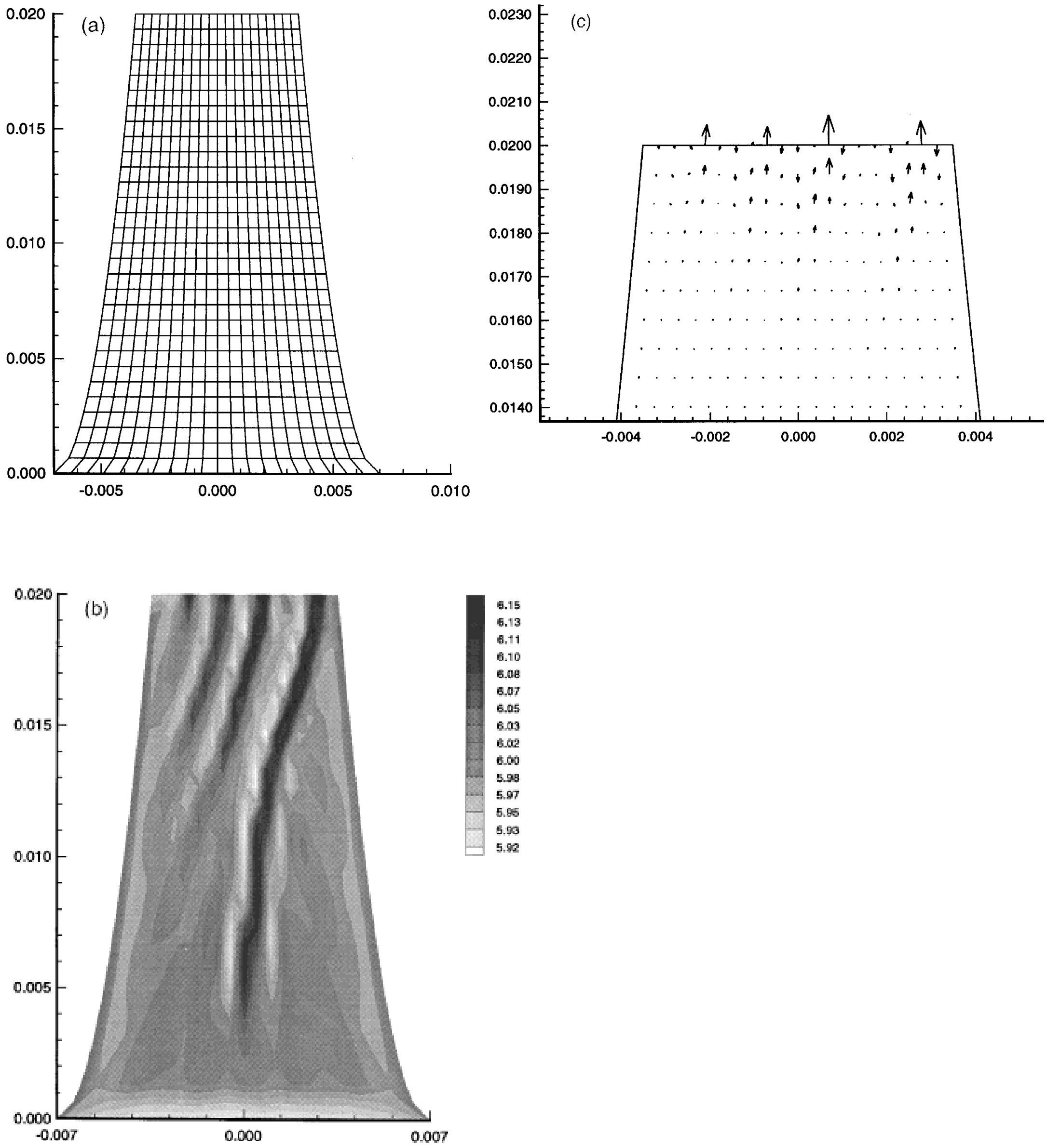

Figure 6. Solidification of Ni–6 wt.% Al–6 wt.% Ta–8 wt.% Cr in a mould contracting smoothly upwards after 200 s: (a) geometry and mesh; (b) mixture concentration of wt.% Al; (c) detail of flow field at top of container (maximum velocity $4 \times 10^{-4}$ mm/s$^{-1}$; fraction of liquid at top, 0·45). Dimensions in metres

rate at the bottom is $r = -0{\cdot}28$ K s$^{-1}$. Figure 6 shows results for a mould contracting from 14 mm at the bottom to 7 mm at the top. At $t = 400$ s the mushy zone has already reached the top of the container. Figure 6(a) shows the mesh, Figure 6(b) shows the concentration of aluminium and Figure 6(c) shows a detail of the velocity field at the top of the container, where a zero-normal-stress boundary condition was applied. Note that the magnitude of the velocities is very small because the fraction of liquid is already less than 0·5. The first channel starts approximately 4 mm from the

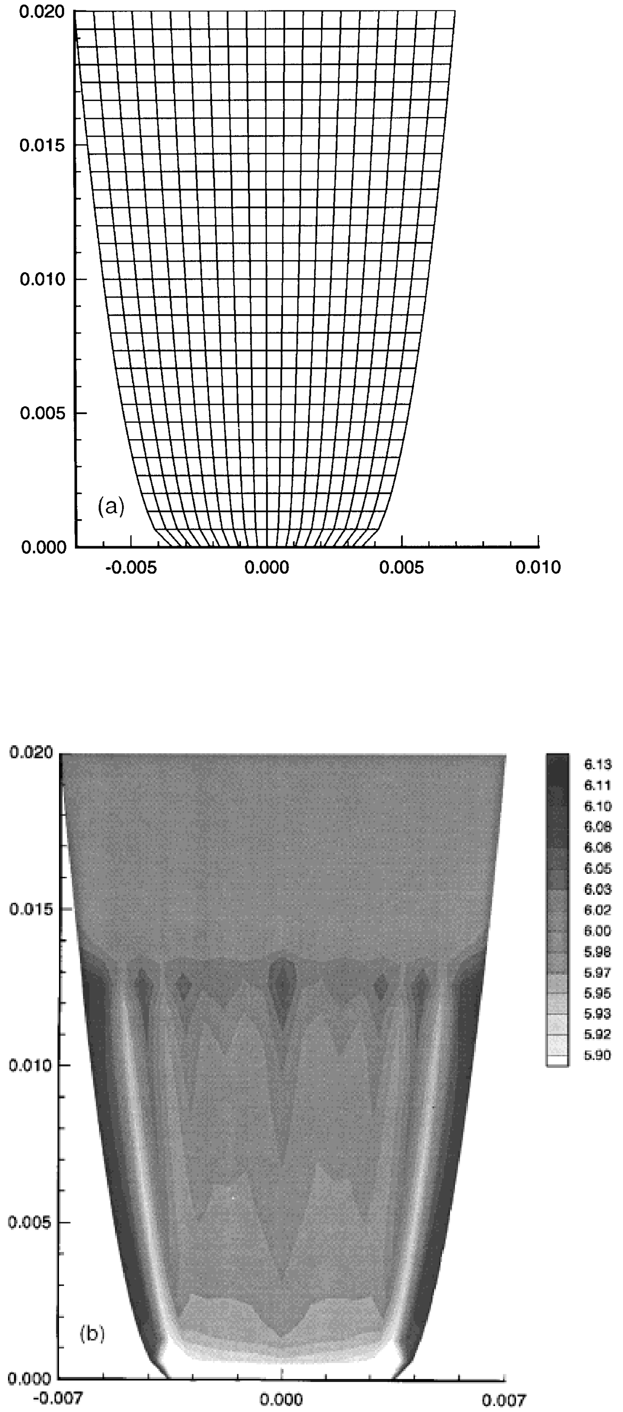

Figure 7. Solidification of Ni–6 wt.% Al–6 wt.% Ta–8 wt.% Cr in a mould diverging smoothly upwards after 200 s: (a) geometry and mesh; (b) mixture concentration of wt.% Al; (c) flow field (maximum velocity 0·5 mm $s^{-1}$). Dimensions in metres

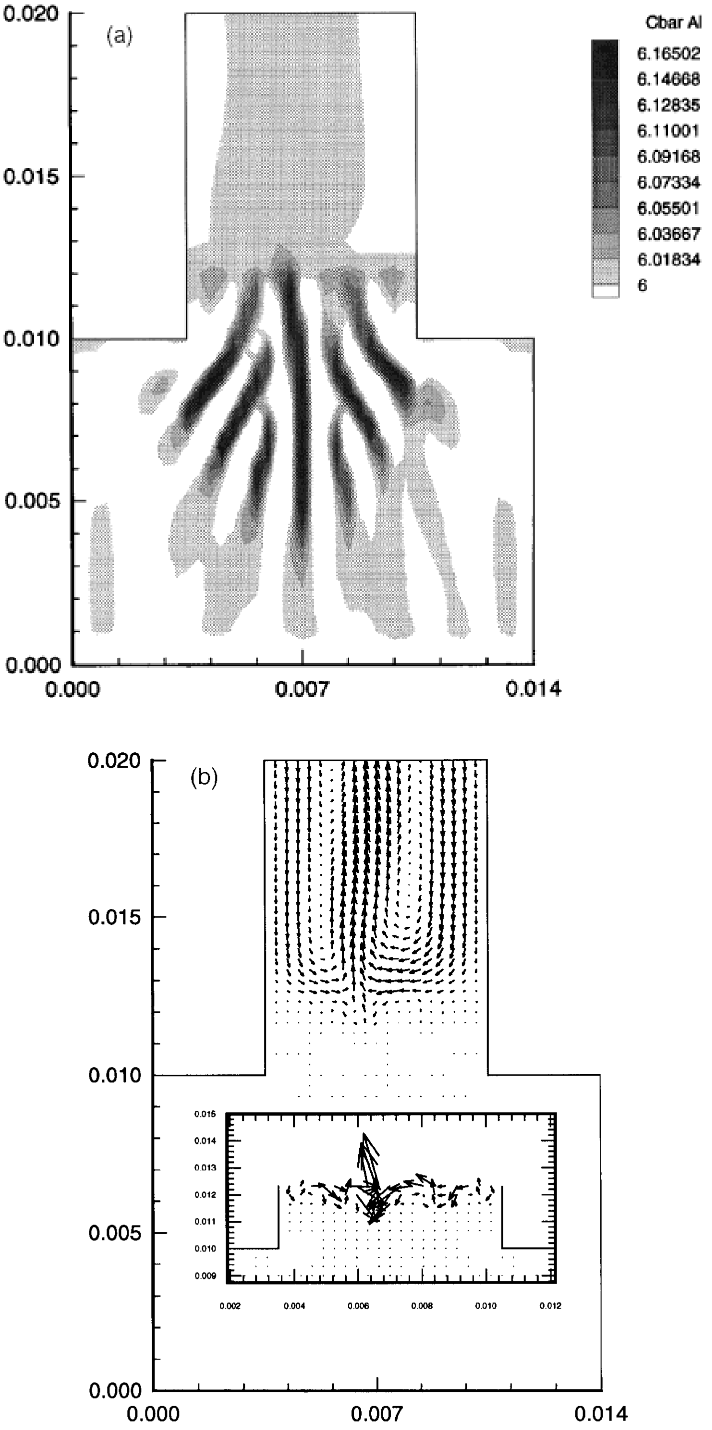

Figure 8. Solidification of Ni–6 wt.% Al–6 wt.% Ta–8 wt.% Cr in a mould with a sudden contraction after 200 s: (a) concentrations above 6% of wt.% Al in the mixture (positive segregation only); (b) flow field with detail at the top of the mushy zone (maximum velocity 0·2 mm $s^{-1}$). Dimensions in metres

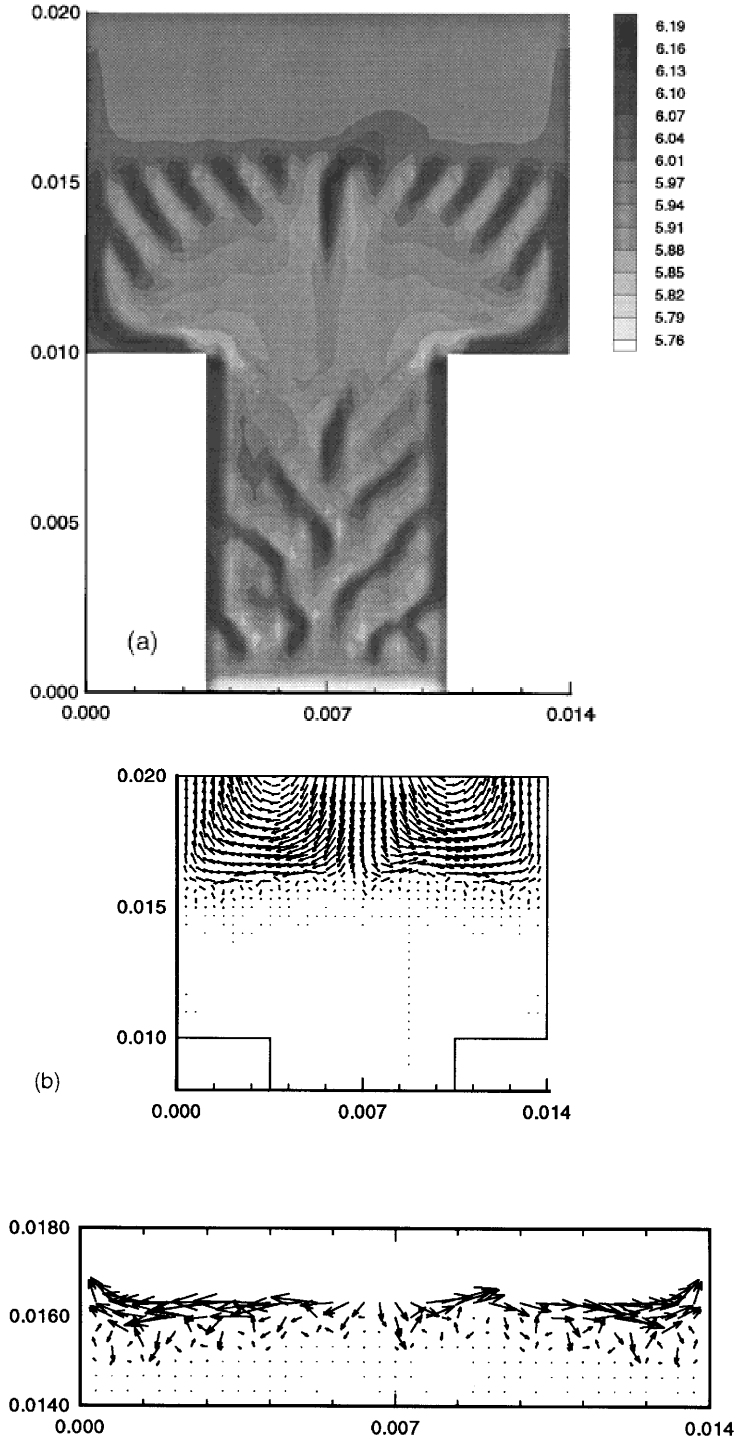

Figure 9. Solidification of Ni–6 wt.% Al–6 wt.% Ta–8 wt.% Cr in a mould with a sudden expansion after 200 s: (a) mixture concentration of wt.% Al; (b) flow field with detail at top of mushy zone (maximum velocity 0·4 mm s$^{-1}$). Dimensions in metres

bottom and more channels start developing later at approximately 14 mm from the bottom. This is possibly due to the fact that the solidification speed changes as the container becomes smaller and less energy needs to be extracted to cool the casting. The velocity field in Figure 6(c) shows that all four channels at the top are of about equal strength and within the mushy zone. In this case the channels have aligned themselves towards the right wall of the container owing to the convection in the all-liquid region during solidification.

Figure 7 shows the mesh and results at $t = 400$ s for a mould expanding smoothly from 7 mm at the bottom to 14 mm at the top. Segregation is confined mainly to the side walls (Figure 7(b)); however, as shown in Figure 7(c), the flow appears to be driven mainly by natural convection along the walls and almost no interaction with the mushy zone is apparent, except near the side walls. Notice also that the leading part of the mushy zone has only reached approximately 13 mm from the bottom because less energy can be extracted through the smaller bottom surface and hence the speed of solidification is much lower in this case.

### *4.3. Solidification in Enclosures with Abrupt Changes in Geometry (Cases 4 and 5)*

The effect that abrupt changes in geometry have on the convection during solidification is illustrated using the same alloy and solidification conditions as in Section 4.2, with abrupt expansion and contraction part way up the container. The calculations were performed using a square regular mesh of size $\Delta x = \Delta y = 0{\cdot}35$ mm.

Results after 200 s of solidification are shown in Figures 8 and 9, where the geometry of the container is defined. In Figure 8(a), which shows regions with only positive segregation of aluminium, the contraction enhances the formation of internal channels. As the mushy zone advances towards the step, convection is very strong in the neck but only one of the plumes escapes to the liquid and the others turn back, as shown in detail in Figure 8(b). Finally, Figure 9(a) shows that an expansion acts as an inhibitor to the formation of internal channels; the segregation pattern in the bottom half was broken by the sudden expansion and segregation relegated to the corners and the walls. However, after a while, channels develop again. The convective field in Figure 9(b) shows that convection is weak and does not penetrate the mushy zone. In fact, the flow in all 10 upward-flowing locations turns very close to the mushy zone, creating small recirculating cells similar to those shown in Figures 5(a) and 8(b).

## 5. CONCLUSIONS

A finite element model of the solidification of dendritic multicomponent alloys has been constructed to study macrosegregation resulting from the convection that develops in the melt during the solidification process. The two-dimensional model has allowed us to study in detail the mechanisms that produce convection in the melt and the effect of convection on macrosegregation. In particular, we have been able to determine that freckles are a direct consequence of flow instabilities in the mushy zone. Given the sensitivity of the resulting convection to changes in some of the physical parameters, we have demonstrated the need for a comprehensive database in the future as models of this type are used in the design of casting processes. The model has been extended to three dimensions and preliminary calculations show that the two-dimensional model is at least qualitatively correct in its predictions.

### ACKNOWLEDGEMENTS

This work was supported by the Advanced Research Projects Agency under the Micromodeling Program of the Investment Casting Cooperative Arrangement under contract MDA972-93-2-0001 and by the National Aeronautics and Space Administration, Microgravity Division, under contract

NCC8-96. The provision of financial support for Dr. S. Felicelli by the Consejo Nacional de Investigaciones Cientificas y Tecnicas (CONICET, Argentina) and the Argentina Atomic Energy Commission is gratefully acknowledged.

## REFERENCES

1. M. McLean, *Directionally Solidified Materials for High Temperature Service*, The Metals Society, London, 1983, pp. 1–8.
2. A. F. Giamei and B. H. Kear, ‘On the nature of freckles in nickel base superalloys’, *Metall. Trans.*, **1**, 2185–2192 (1970).
3. S. M. Copley, A. F. Giamei, S. M. Johnson, and M. F. Hornbecker, ‘The origin of freckles in unidirectionally solidified castings’, *Metall. Trans.*, **1**, 2193–2204 (1970).
4. C. F. Chen and F. Chen, ‘Experimental study of directional solidification of aqueous ammonium chloride solution’, *J. Fluid Mech.*, **227**, 567–586 (1991).
5. R. Mehrabian and M. C. Flemings, ‘Macrosegregation in ternary alloys’, *Metall. Trans.*, **1**, 455–464 (1970).
6. T. Fujii, D. R. Poirier and M. C. Flemings, ‘Macrosegregation in a multicomponent low alloy steel’, *Metall. Trans. B*, **10**, 331–339 (1979).
7. A. L. Maples and D. R. Poirier, ‘Convection in the two-phase zone of solidifying alloys’, *Metall. Trans. B*, **15**, 163–172 (1984).
8. G. B. McFadden, R. G. Rehm, S. R. Coriell, W. Chuck and K. A. Morrish, ‘Thermosolutal convection during directional solidification’, *Metall. Trans. A*, **15**, 2125–2137, (1984).
9. J. C. Heinrich, ‘Numerical simulation of thermosolutal instability during directional solidification of a binary alloy’, *Comput. Methods Appl. Mech. Eng.*, **69**, 659–671 (1988).
10. V. R. Voller and C. Prakash, ‘A fixed grid numerical modelling methodology for convection diffusion mushy region phase change problems’, *Int. J. Heat Mass Transfer*, **30**, 1709–1719 (1984).
11. W. D. Bennon and F. P. Incropera, ‘The evolution of macrosegregation in statically cast binary ingots’, *Metall. Trans. B*, **18**, 611–616 (1987).
12. C. Beckermann and R. Viskanta, ‘Double-diffusive convection during dendritic solidification of a binary mixture’, *Phys.-Chem. Hydrodyn.*, **10**, 195–213 (1988).
13. J. C. Heinrich, S. D. Felicelli, P. Nandapurkar and D. R. Poirier, ‘Thermosolutal convection during dendritic solidification of alloys: Part II. Nonlinear convection’, *Metall. Trans. B*, **20**, 883–891 (1989).
14. S. D. Felicelli, J. C. Heinrich and D. R. Poirier, ‘Simulation of freckles during vertical solidification of binary alloys’, *Metall. Trans. B*, **22**, 847–859 (1991).
15. S. D. Felicelli, J. C. Heinrich and D. R. Poirier, ‘Numerical model for dendritic solidification of binary alloys’, *Numer. Heat Transfer.*, **23**, 461–481 (1993).
16. M. C. Schneider and C. Beckermann, ‘Formation of macrosegregation by multicomponent thermosolutal convection during the solidification of steel’, *Metall. Mater. Trans. A.*, **26**, 2373–2388 (1995).
17. S. D. Felicelli, D. R. Poirier and J. C. Heinrich, ‘Macrosegregation patterns in multicomponent Ni-base alloys’, *J. Cryst. Growth*, in press.
18. S. D. Felicelli, D. R. Poirier, A. F. Giamei and J. C. Heinrich, ‘Simulation of the solidification of DS and SC superalloys’, *J. Met.*, **49**, 21–25 (1997).
19. D. R. Poirier, ‘Permeability of flow of interdendritic liquid in columnar-dendritic alloys’, *Metall. Trans. B*, **18**, 245–255 (1987).
20. M. S. Bhat, D. R. Poirier and J. C. Heinrich, ‘Permeability of cross flow through columnar dendritic alloys’, *Metall. Trans. B*, **26**, 1049–1056 (1995).
21. J. Donea, S. Giuliani and H. Laval, ‘Finite element solution of the unsteady Navier–Stokes equations by fractional step method’, *Comput. Methods. Appl. Mech. Eng.*, **30**, 53–73 (1982).
22. L. Quartapelle, *Numerical Solution of the Navier–Stokes Equations*, Birkhauser, Boston, MA, 1993.
23. T. J. R. Hughes and L. P. Franca, ‘A new finite element formulation for computational fluid dynamics; VII. The Stokes problem with various well-posed boundary conditions: symmetric formulations that converge for all velocity/pressure spaces’, *Comput. Methods. Appl. Mech. Eng.*, **65**, 85–96 (1987).
24. L. P. Franca and S. L. Frey, ‘Stabilized finite element methods; II. The incompressible Navier–Stokes equations’, *Comput. Methods. Appl. Mech. Eng.*, **99**, 209–233 (1992).
25. S. D. Felicelli, ‘Simulation of freckles during vertical solidification of binary alloys’, *Ph.D. Dissertation*, University of Arizona, Tucson, AZ, 1991.
26. P. W. Peterson, T. Z. Kattamis and A. F. Giamei, ‘Coarsening kinetics during solidification of Ni–Al–Ta dendritic monocrystals’, *Metall. Trans. A*, **11**, 1059–1065 (1980).
27. *Metals Handbook*, Vol. 8, 8th edn., American Society for Metals, Metals Park, OH, 1974.
28. R. Kadalbar, J. J. Montoya-Cruz and T. Z. Kattamis, ‘Solute redistribution during and after solidification of Ni–Al–Ta dendritic monocrystals’, *Metall. Trans. A*, **11**, 1547–1553 (1980).
29. S. N. Tewari, M. Vijayakumar, J. E. Lee and P. A. Curreri, ‘Solutal partition coefficients in nickel-base superalloy PWA-1480’, *Mater. Sci. Eng. A*, **141**, 97–102 (1991).

30. D. Poirier and E. McBride, ‘Estimating the densities of the liquid transitional metals and Ni–Al–Cr–Ta alloys’, *Internal report under Investment Casting Cooperative Agreement*, Department of Materials Science and Engineering, University of Arizona, Tucson, AZ, 1996.
31. T. Iida and R. I. L. Guthrie, *The Physical Properties of Metals*, Oxford University Press, Oxford, 1988, pp. 8, 9, 183).
32. A. Goldsmith, T. E. Waterman and H. J. Hirschhorn, *Handbook of Thermophysical Properties of Solid Materials*, Vol. I, McMillan., New York, 1961, p. 449.